Supporting Information

Multi-objective collaborative design optimized highly efficient energy capacitive lead-free relaxor ferroelectrics

Long Lin,[a] Chongyang Li,[a] Yibo Zhang,[a] Wangfeng Bai,[a,b*] Shiting Wu,[a] Yongjun Yuan,[a] Wei Li,[c] Jiwei Zhai[d*]

[a] College of Materials and Environmental Engineering, Hangzhou Dianzi University, No. 2 Street, Hangzhou 310018, China

[b] Key Laboratory of Novel Materials for Sensor of Zhejiang Province, Hangzhou Dianzi University, Hangzhou 310012, China

[c] School of Materials Science and Engineering, Liaocheng University，Liaocheng 252059, China

[d] Functional Materials Research Laboratory, School of Materials Science & Engineering, Tongji University, No. 4800 Caoan Highway, Shanghai, 201804, China

* Corresponding author.   E-mail address: bwfcxj@126.com (W. Bai), apzhai@tongji.edu.cn (J. Zhai).

Experimental section

Ceramic preparation:

$(1-x)[0.955(Bi_{0.5}Na_{0.5}TiO_3)-0.045Ba(Al_{0.5}Ta_{0.5})O_3]-xNaTaO_3$ (abbreviated as BNT-BAT-xNT, x=0.05, 0.1, 0.15, 0.2) ceramics were prepared by conventional solid phase method with high purity Bi_2O_3, Na_2CO_3, TiO_2, $BaCO_3$, Al_2O_3, Ta_2O_5 ($\geq$ 99%) as raw materials. The above powders were weighed according to stoichiometric ratio and ball milled for 24 h. The obtained BNT-BAT powders were calcined at 850 °C for 6 h, and the NT powders were calcined at 800 °C for 4 h. Then the BNT-BAT and NT powders were mixed and ball milled for 48 h. The resulting powders were mixed with 8 wt% organic binders (PVA) for granulation, and then pressed into pellets with a diameter of 10 mm and a thickness of 1 mm. Ultimately, the pressed disks were sintered at 1125-1175 °C for 2 h.

Structure characterizations:

The X-ray diffractometer (XRD; MiniFlex600, Rigaku, Japan) and Raman spectra (Horiba/Jobin Yvon, Villeneuve d'Ascq, France) were employed to analyze the phase structure. The sample microstructure was observed by the field emission scanning electron microscope (FE-SEM, S-4200, Hitachi, Tokyo, Japan). The domain morphology and high-resolution atomic imaging of ceramics were observed via field emission transmission electron microscopy (TEM; FEI Talos F200X, USA) at an accelerated voltage of 200 kV. To collect domain morphology and dynamic response, Piezoresponse force microscopy (PFM) measurements of ceramics were performed using an atomic force microscopy (AsylumResearch MFP-3D).

Electrical properties:

To perform energy storage measurements, the sintered ceramics were grinded and polished to approximate 50-80 μm in thickness and then sputtered with gold electrodes. The polarization hysteresis (*P-E*) loops with respect to temperature, frequency, cycles and the FORC loops were measured via an FE test system (RT1-Premier II, Radiant Technologies InC, USA). The temperature and frequency dependence of dielectric constant and loss were examined using a high-precision LCR meter (HP 4990 A;

Agilent, Palo Alto, CA). The charging-discharging performance of ceramic capacitors was estimated via a commercial charge-discharge platform (CFD-003, Gogo Instruments Technology, China) with a certain discharge resistance, inductance, and capacitance load circuit. The absorption spectrum was collected using an ultraviolet spectrophotometer (TU-1901, Beijing Purkinje General Instrument, China).

The FORC distribution:

In this work, E_{max} is set to be 80 kV/cm, $\Delta\alpha = \Delta\beta = \Delta E = 4$ kV/cm. An approximate method to calculate $p(\alpha, \beta)$ is

$$p(\alpha,\beta) = \frac{1}{2}\frac{\partial p^2(\alpha,\beta)}{\partial\alpha\partial\beta} \#(1)$$

where $p(\alpha, \beta)$ is the polarization of the FORC loop, α is the reversal electric field, and β is the real electric field [1].

Finite Element Simulation:

To better understand the dielectric breakdown process, finite element analysis was used to simulate the distributions of electric potential, electric field, and polarization with the evolution of the electrical tree. According to the experimental SEM images, two-dimensional simulation model was established. The probability of the electrical tree channels was calculated using the following equation [2, 3]:

$$p(i^{'},j^{'}\rightarrow i,j) = \frac{\left(\emptyset_{i^{'},j^{'}} - \emptyset_{i,j} - \emptyset\right)^m}{\sum\left(\emptyset_{i^{'},j^{'}} - \emptyset_{i,j} - \emptyset\right)^m} + \left(\emptyset_{i^{'},j^{'}} - \emptyset_{i^{''},j^{''}} - \emptyset\right)^m - loss\#(2)$$

where $\emptyset_{i,j}$, $\emptyset_{i^{'},j^{'}}$ and $\emptyset_{i^{''},j^{''}}$ represent the electrical potential of the discharged point, probable point, and linked point, respectively. $\emptyset$ is the threshold electrical potential of the ceramic for grain and grain boundary. m is the fractal dimension. loss denotes the evolution loss of the tip electrical tree channels.
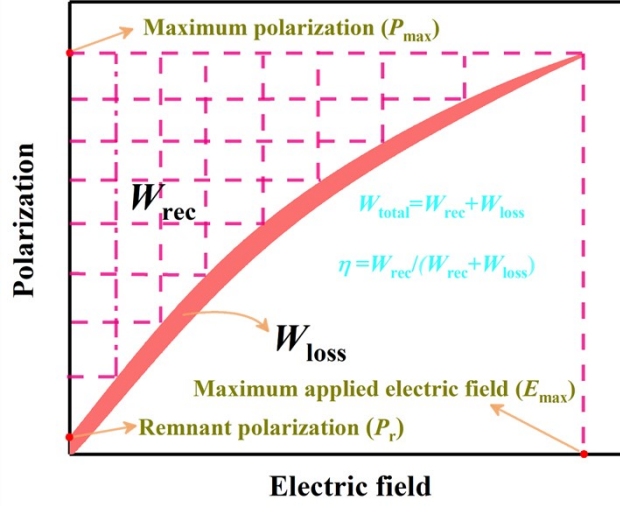
**Fig. S1** Graphical representation of polarization-electric field (*P-E*) hysteresis loop for energy-storage calculation.

The total energy density (W_{total}), recoverable energy density (W_{rec}), and energy efficiency (η) of dielectric capacitors can be calculated by the three formulas, which are expressed as follows [4, 5]:

$$W_{total} = \int_{0}^{P_{max}} Edp \#(3)$$

$$W_{rec} = \int_{P_r}^{P_{max}} Edp \#(4)$$

$$\eta = \frac{W_{rec}}{W_{total}} \times 100\% \#(5)$$

where P_{max}, P_r, and E denote the maximum polarization, remnant polarization, and electric field strength, respectively. As shown in Fig. S1, in order to achieve excellent ESP, the P_{max} and breakdown strength (E_b) must be improved, and P_r must be reduced while delaying the saturation polarization [6, 7].
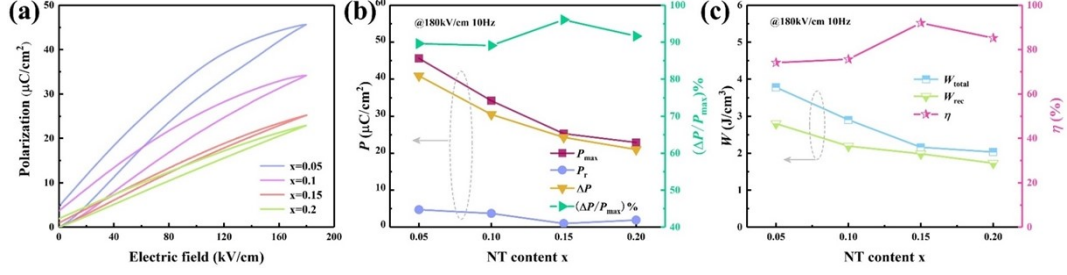
Fig. S2 (a) Unipolar $P\text{-}E$ loops, (b) changes of P_{max}, P_r, ΔP and $\Delta P/P_{max}$, and (c) W_{total}, W_{rec} and η of the BNT-BAT-xNT ceramics under 180 kV/cm and 10 Hz.

In order to determine the phase transition, the unipolar $P\text{-}E$ curves of BNT-BAT-xNT ceramics are recorded under 180 kV/cm and 10 Hz. Obviously, with the increase of NT content, the $P\text{-}E$ curve gradually becomes slender, and P_{max} and P_r decrease at the same time, indicating the disrupted long-range ferroelectric order and decreased energy loss. For x=0.05, the phase structure is NR-ER phase at room temperature, leading to high $P_{max,}$ large P_r, obvious hysteresis, and significantly early polarization saturation. In the case of x=0.15, the room temperature phase structure is dominated ER, which can disrupt long-range ferroelectric order and induce PNRs, thus generating a slim $P\text{-}E$ loop with an ultralow P_r, a relatively high P_{max}, and significantly delayed polarization saturation. In consequence, the P_{max} decreases markedly for x $\geq$ 0.15. Furthermore, $\Delta P/P_{max}$ under 180 kV/cm for x=0.15 behaves a highest value compared with other compositions, which is the key contribution of polarization. Excitingly, the smallest P_r (< 1 $\mu C/cm^2$) and the largest $\Delta P/P_{max}$ (%) (> 95%) while maintaining a large ΔP (> 20 $\mu C/cm^2$) are realized simultaneously in x=0.15 ceramic, resulting in the optimized W_{rec} and η.
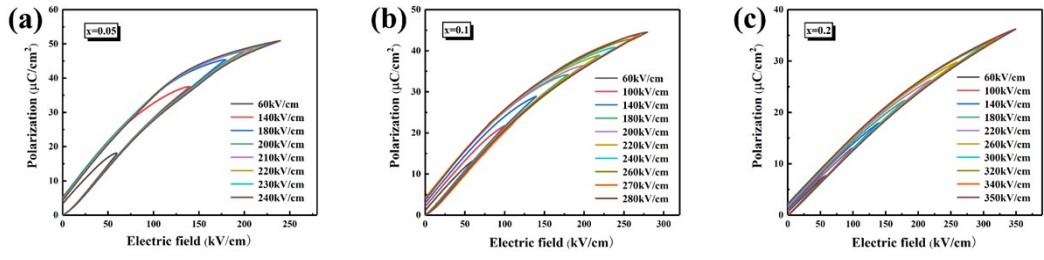
Fig. S3 *P-E* loops measured at 10 Hz for BNT-BAT-xNT ceramics: (a) x = 0.05, (b) x = 0.1, and (c) x = 0.2.
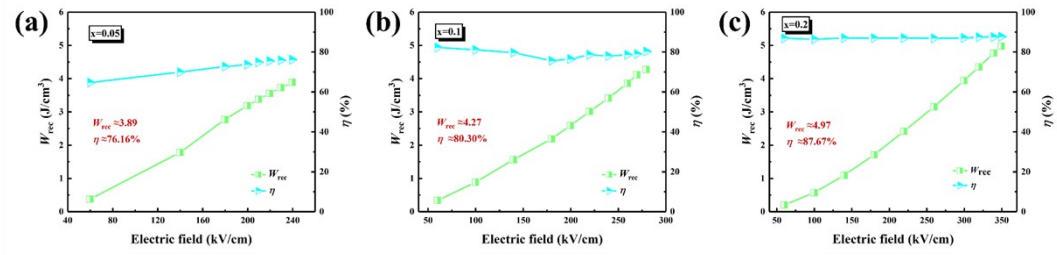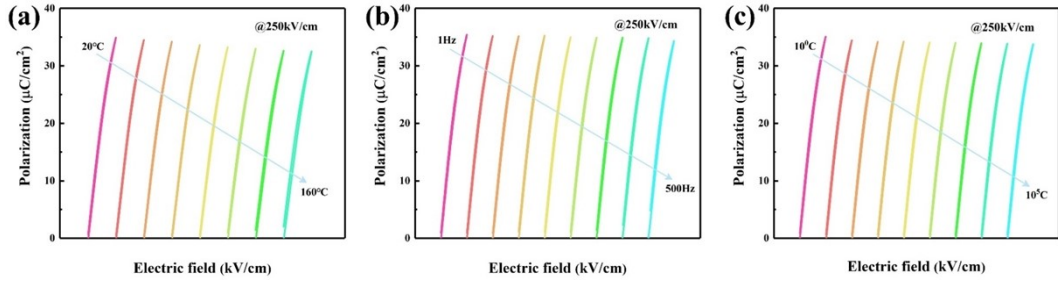
Fig. S4 The W_{rec} and η for BNT-BAT-xNT ceramics: (a) x = 0.05, (b) x = 0.1, and (c) x = 0.2.
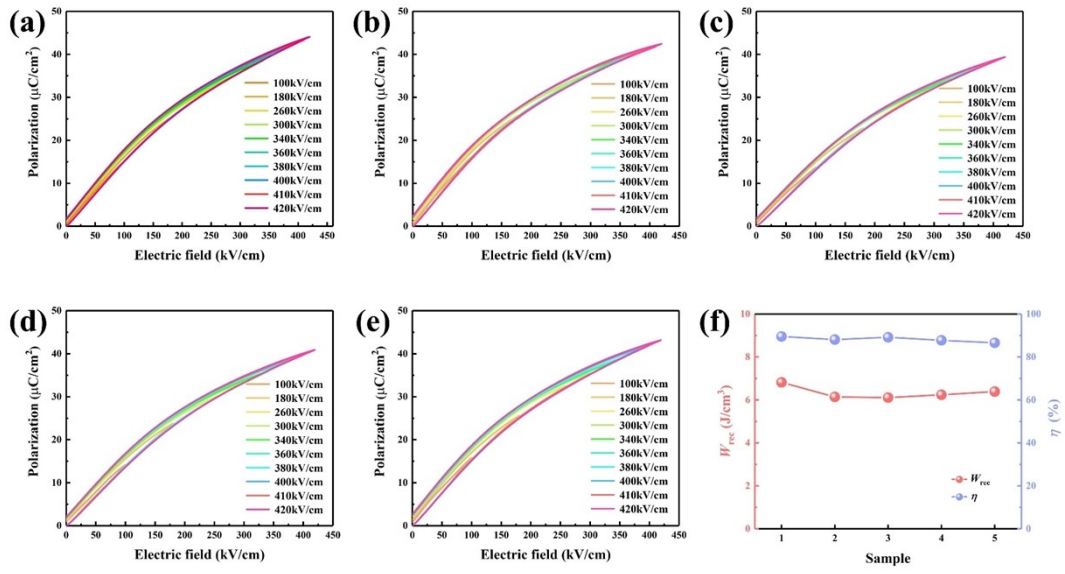
**Fig. S5** (a)-(e) *P-E* loops of five x=0.15 ceramics, and (f) the corresponding variation of W_{rec} and η of five samples.

Fig. S6 (a) Temperature-, (b) frequency-, and (c) cycle number- dependent unipolar *P-E* loops measured under 250 kV/cm for x=0.15 ceramic.

Clearly, the W_{rec} and η keep stable in the whole frequency range. On the one hand, this is mainly linked with the reduced loss resulted from the weakening of polarization relaxation phenomenon at low frequency (see Fig. 4(g)) [8]. As demonstrated in Fig. 5, the weakly coupled PNRs would generate a fast response of each PNR during electric field loading, leading to near-zero P_r and high η with frequency [9]. On the other hand, as shown in Fig. 4(h), dielectric constant decreases with increasing frequency, which can reduce the P_{max} values and thus produce a slight reduction in W_{rec} (see Fig. 3(b)). As a result, the η keeps stable and the W_{rec} decreases slightly with increasing the frequency.
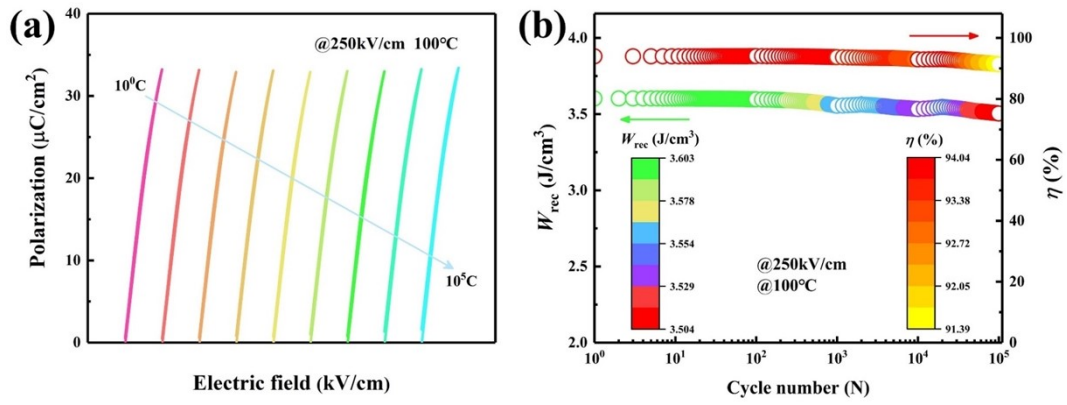
Fig. S7 (a) The cycle number dependence of unipolar P-E loops, and (b) W_{rec} and η measured under 250 kV/cm and 100 °C up to 10^5 cycles for x=0.15 ceramic.
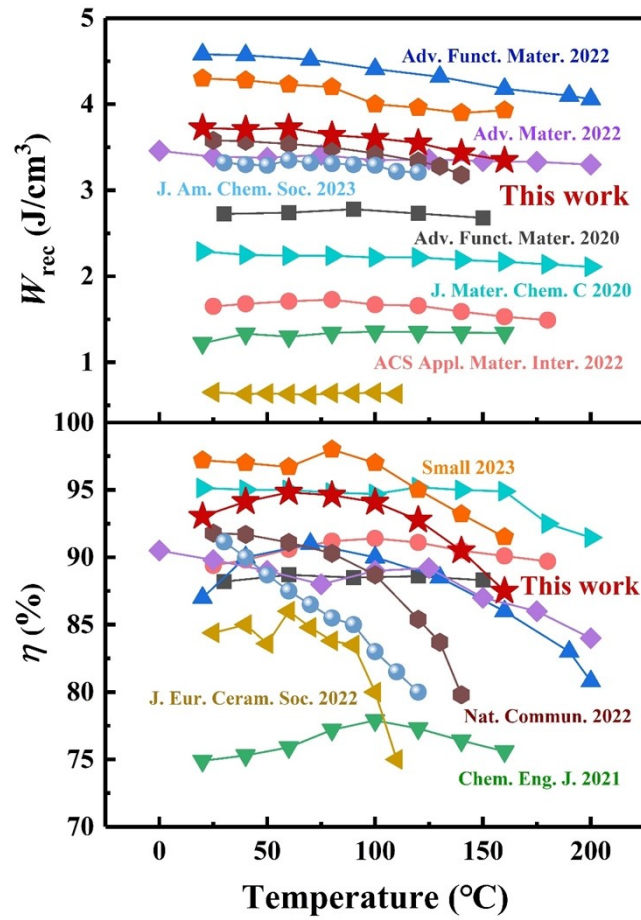
Fig. S8 A comparison of temperature stability of W_{rec} and η in various representative lead-free energy storage ceramics. The references are listed in Table S2.
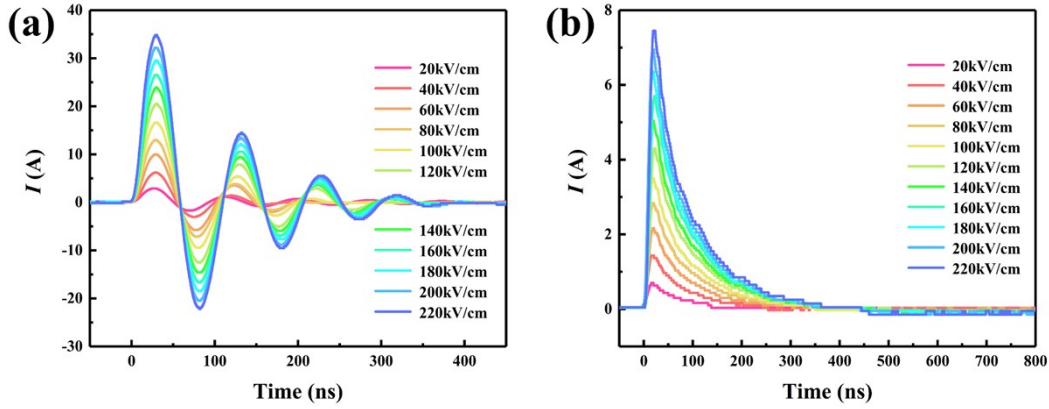
Fig. S9 (a) Underdamped discharge waveforms and (b) overdamped discharge waveforms for x=0.15 ceramic.

Fig. S9 shows underdamped and overdamped discharge waveforms for x=0.15 ceramic. As shown in Fig. 2(d) and Fig. 3(e), it has a certain degree of difference between W_d and W_{rec}, namely, the W_d measured in the RC circuit is smaller than W_{rec} measured by the *P-E* loop under the same electric field. On the one hand, the observed difference is mainly caused by the different mechanisms of the two measurements (quasistatic *P-E* loop, 10^{-1} s; dynamic discharge measurement, 10^{-5} s)[10]. On the other hand, the equivalent series resistor, domain walls movement and measurement frequency also generate the loss of discharged energy[11]. In consequence, the difference between W_d and W_{rec} is available in dielectric materials.
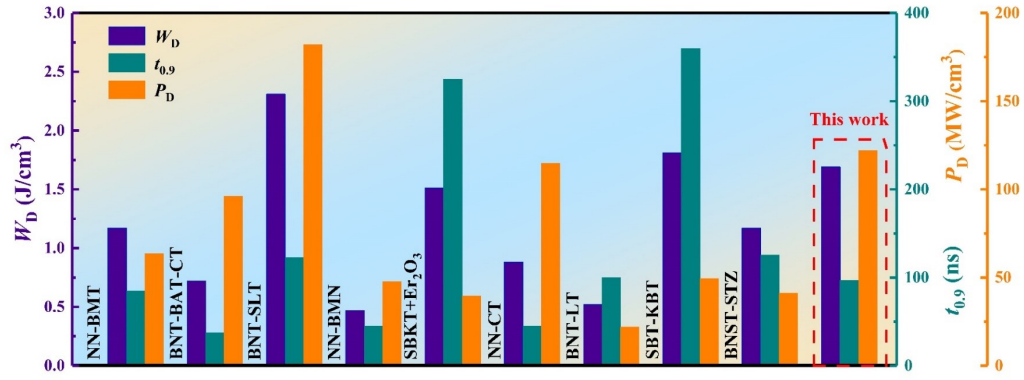
Fig. S10 A comparison of W_D, $t_{0.9}$, and P_D among the x=0.15 ceramic and other representative lead-free systems. The references are listed in Table S3.
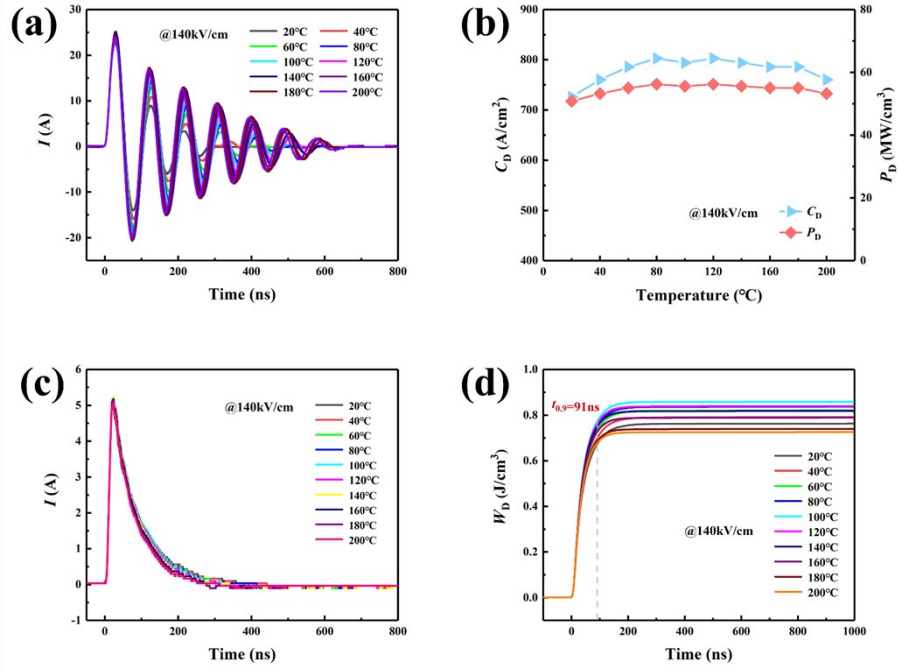
Fig. S11 Temperature-dependent (a) underdamped discharge curves, (b) the changes in C_D and P_D at different temperatures, (c) overdamped discharge curves, and (d) W_D-t curves for x=0.15 ceramic.

The current density (C_D) and power density (P_D) of the sample can be expressed by the following equations [12, 13]:

$$C_D = \frac{I_{max}}{S} \#(6)$$

$$P_D = \frac{EI_{max}}{2S} \#(7)$$

where I_{max}, S and E are the first current peak amplitude, electrode area, and electric field strength, respectively. The discharge energy density (W_D) can be calculated by the following equation [9, 14]:

$$W_D = \frac{R \int I^2(t)dt}{V} \#(8)$$

where R and V are the total load resistor (200 Ω) and the sample effective volume, respectively. With the increase of temperature (20-200°C), relatively stable underdamped and overdamped waveforms can still be observed. At the same time, the sample maintains a high P_D ($\geq$ 50.8 MW/cm³) and a very short $t_{0.9}$ ($\leq$ 91 ns) at 140 kV/cm, and the change is very small at high temperatures, showing excellent thermal stability of charge/discharge performance.
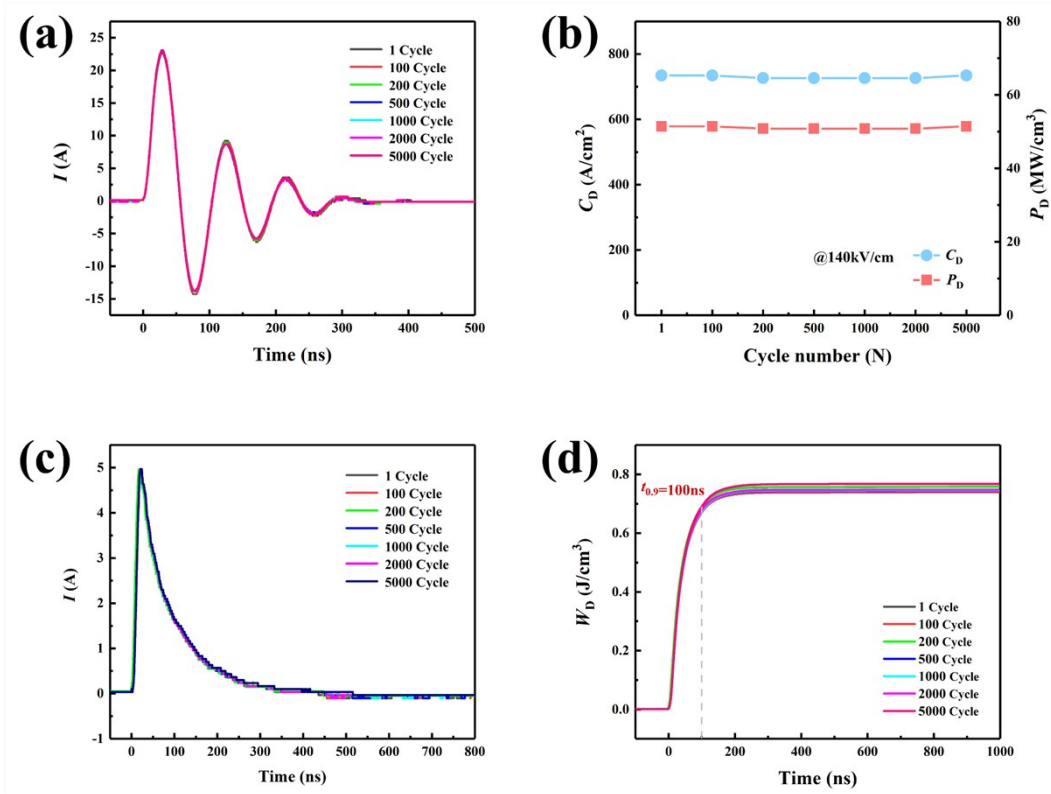
Fig. S12 Cycles-dependent (a) underdamped discharge curves, (b) the changes in C_D and P_D, (c) overdamped discharge curves, and (d) W_D-t curves for x=0.15 ceramic.

After 5000 cycles, the underdamped and overdamped curves of the sample are almost unchanged. A high P_D and a short $t_{0.9}$ can still be maintained. These experimental results show that x=0.15 ceramic has high fatigue reliability.
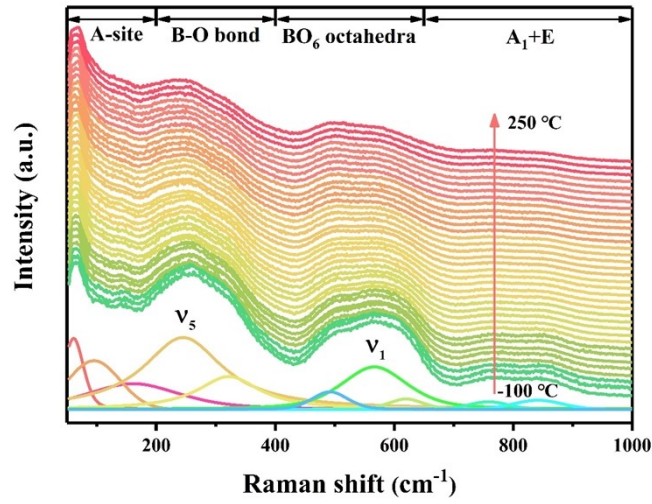
Fig. S13 Evolution of Raman spectra and fitting results for x=0.15 ceramic measured at various temperatures.

Depending on the modes of vibration, the Raman spectra can be separated into four sections (< 200, 200-400, 400-650, and > 650 cm^{-1}) [15].
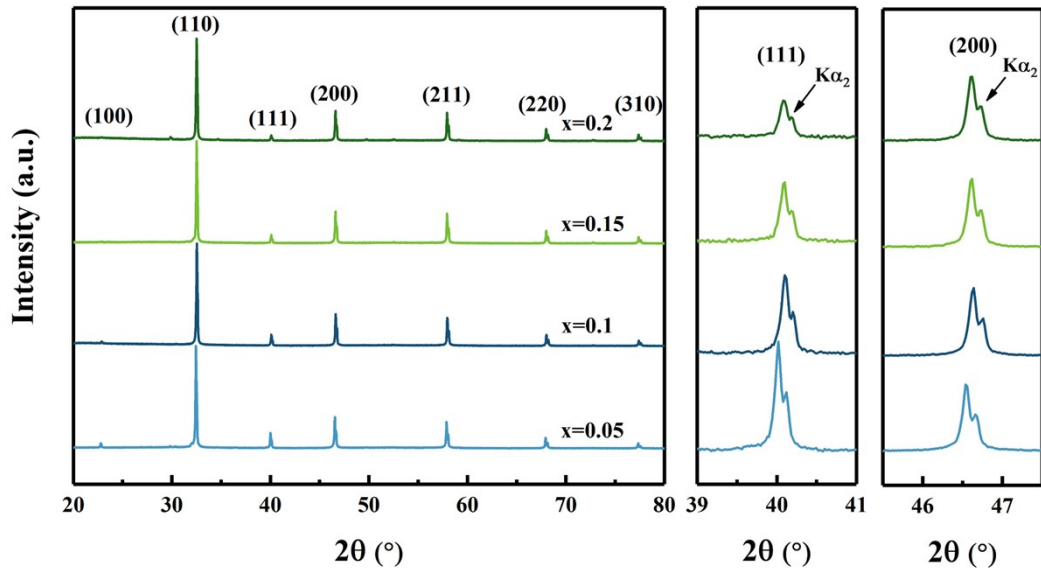
Fig. S14 XRD patterns and enlarged (111) and (200) peaks for BNT-BAT-xNT ceramics.
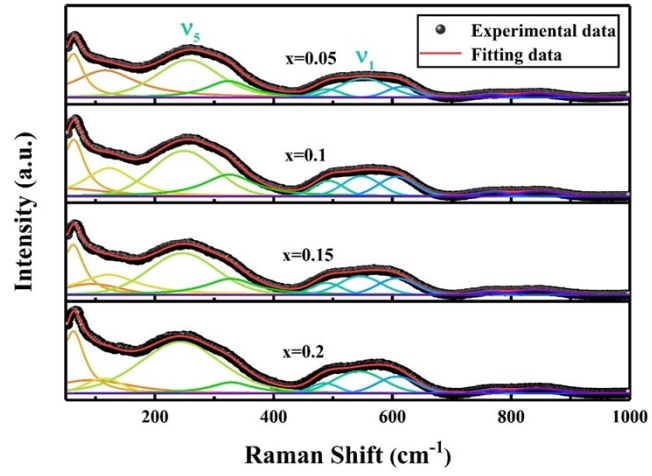
Fig. S15 Raman spectra of BNT-BAT-xNT ceramics.
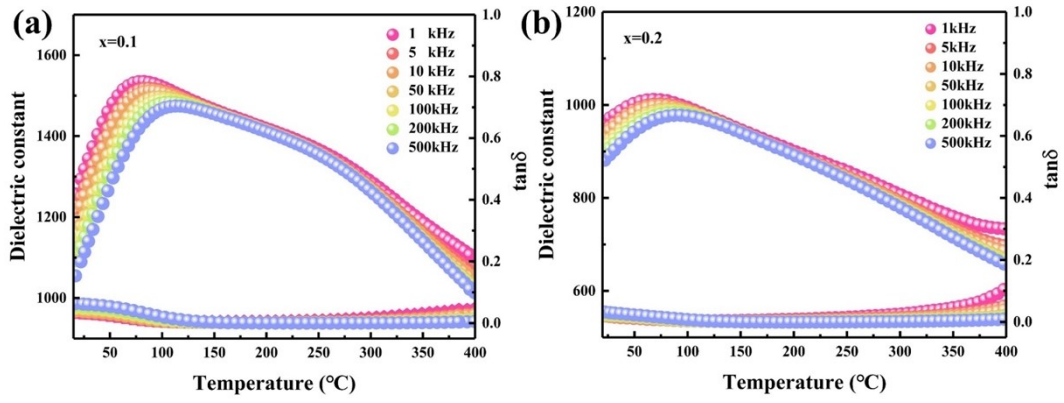
Fig. S16 Temperature dependence of dielectric constant and loss of BNT-BAT-xNT ceramics at various frequencies: (a) x=0.1 and (b) x=0.2.
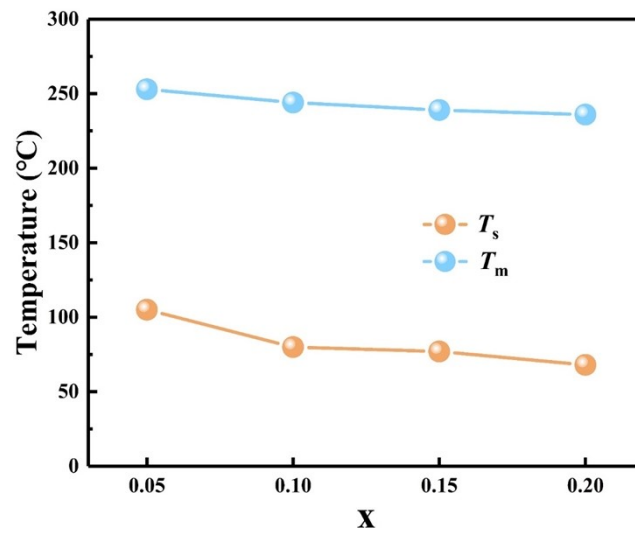
Fig. S17 Phase diagram for BNT-BAT-xNT ceramics.
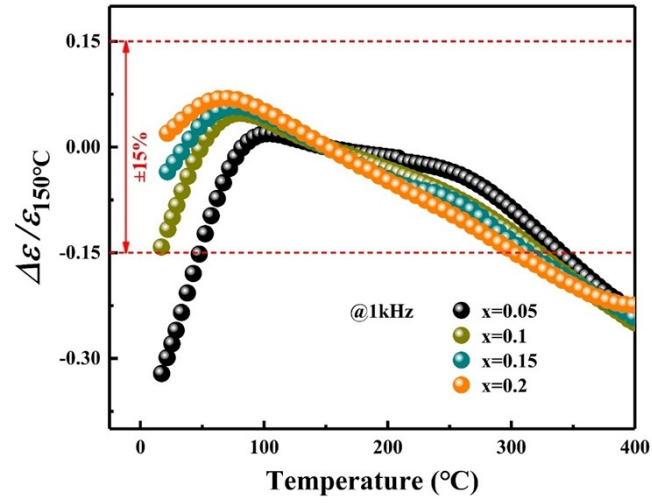
Fig. S18 The thermal stability of dielectric constant ($\Delta\varepsilon/\varepsilon_{150^\circ C}$) for BNT-BAT-xNT ceramics at 1 kHz.
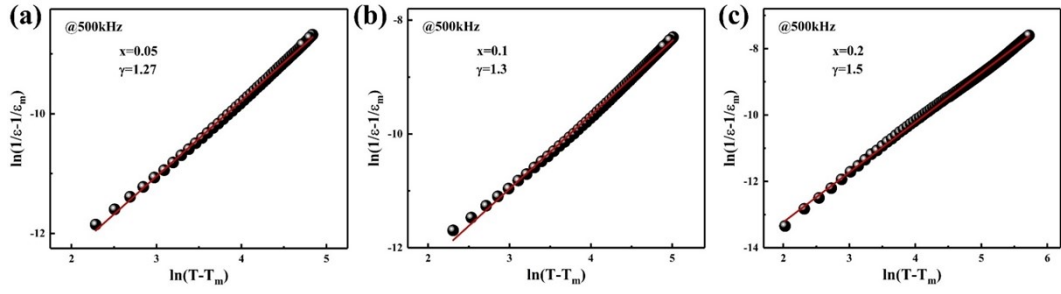
Fig. S19 Diffusion coefficient for BNT-BAT-xNT ceramics: (a) x=0.05, (b) x=0.1, and (c) x=0.2.

The correctional Curie-Weiss relationship is used to more precisely characterize the dielectric relaxation characteristics of the ceramic, and it shows as follows [16]:

$$\frac{1}{\varepsilon_r} - \frac{1}{\varepsilon_m} = \frac{(T - T_m)^\gamma}{C} \#(9)$$

where ε_m represents the maximum ε_r, C is the constant, and γ ($1 \leq \gamma \leq 2$) denotes diffuseness coefficient.
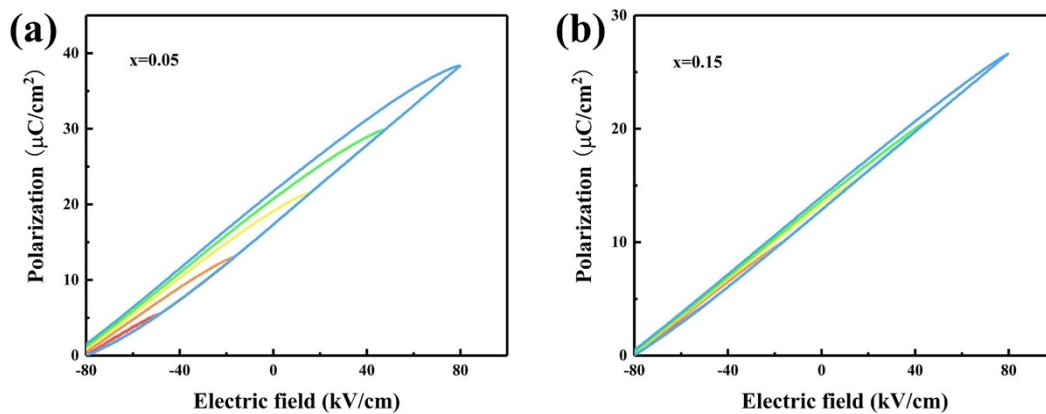
Fig. S20 FORC loops for (a) x=0.05, and (b) x=0.15 ceramic. Only 5 out of the 40 total loops are presented.
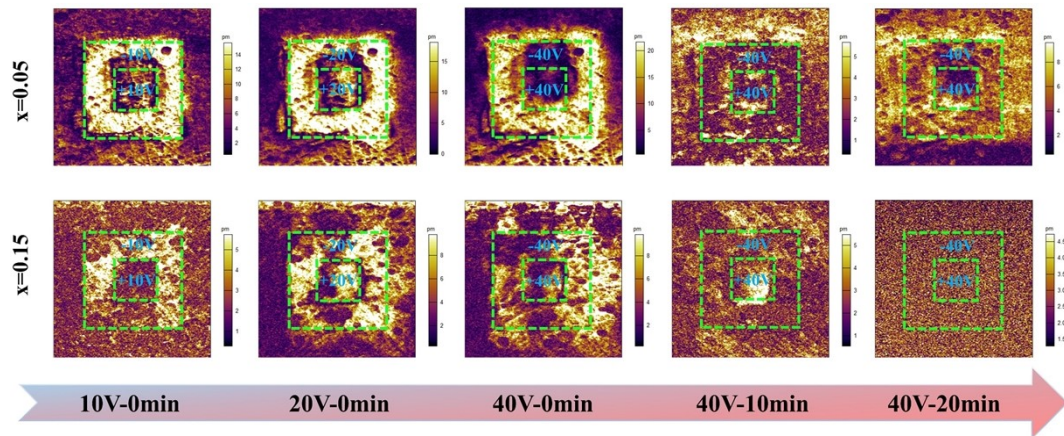
Fig. S21 Out-of-plane PFM amplitude images for indicated ceramics.

Fig. S21 shows the out-of-plane PFM amplitude in the scanning areas of 5×5 μm^2 at different voltages (10V, 20V, 40V) and different relaxation durations (0min, 10min, 20min). A negative DC voltage with different amplitude (-10 V, -20 V, -40V) was applied to the tip of the sample with an area of 3×3 μm^2, and then the same positive DC voltage was imposed on the inner 1×1 μm^2 area to explore the polarization switching behavior.
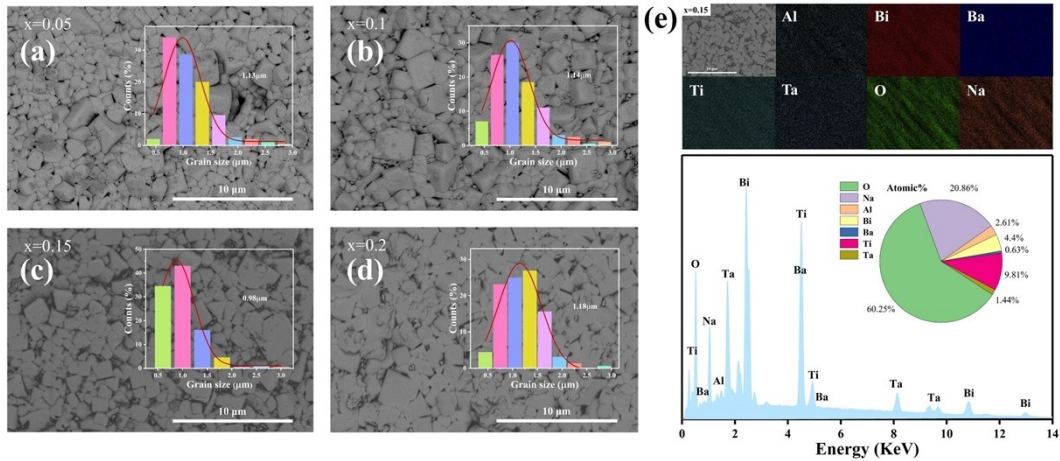
Fig. S22 (a-d) The surface morphology and corresponding grain size distribution of as-sintered BNT-BAT-xNT ceramics; (e) Energy spectrum and atomic proportion of all elements for x=0.15 ceramic.

According to a relationship established by Tunkasiri: $E_b \propto 1/G^{-1/2}$, the small grain size can increase E_b in ceramics [17]. The minimum grain size for x=0.15 ceramic is 0.98 μm, which offers a fundamental assurance for the improvement of E_b. All elements are distributed equally, which demonstrates a high degree of chemical uniformity.
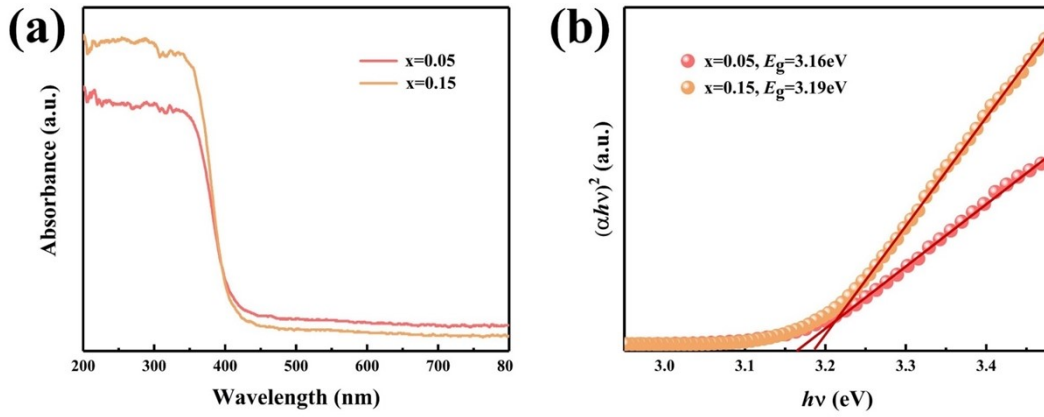
Fig. S23 (a) UV-vis absorbance spectra and (b) $(\alpha h v)^2$ *vs hv* plot for x=0.05 and x=0.15 ceramics.

The band gap (E_g) can be obtained by the Tauc equation:

$$(\alpha h v)^2 = A(h v - E_g) \#(10)$$

where *hv*, *A*, and *α* represent photon energy, a constant, and absorption coefficient, respectively [18]. Having a wide E_g will prevent electrons jumping from the top of the valence band to the bottom of the conduction band [11, 13].
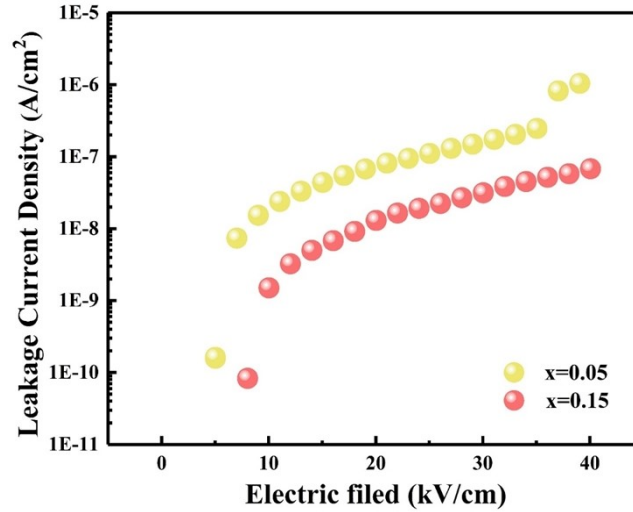
Fig. S24 The leakage current density for x=0.05 and x=0.15 ceramics.

Fig. S24 shows the leakage current density for x=0.05 and x=0.15 ceramics. In general, the increased leakage current is a result of the increasing number and kinetic energy of charged carriers [19, 20]. The low leakage current means the decreasing number and kinetic energy of charged carriers, which generates high E_b for dielectric materials. In this study, compared to x=0.05 ceramic, the x=0.15 ceramic exhibits reduced leakage current density resulted from fewer charge carriers, thus yielding great amplification of E_b [21, 22].
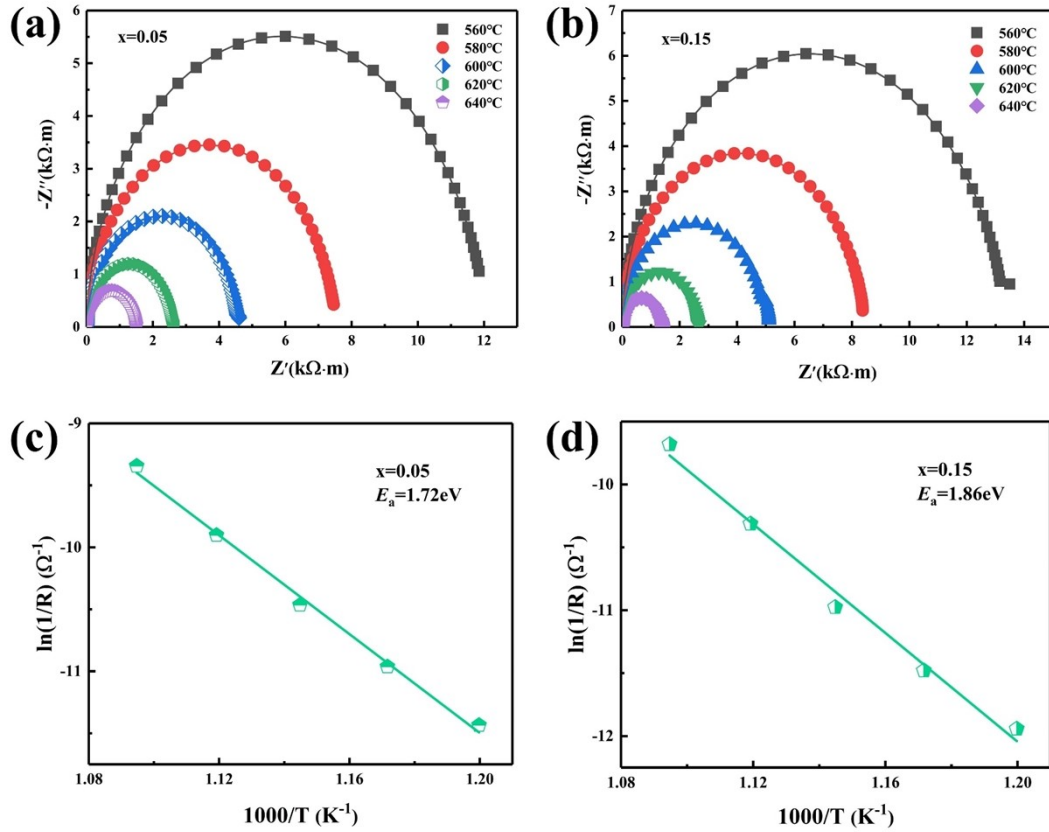
Fig. S25 The complex impedance at various temperatures [(a) and (b)] and activation energy [(c) and (d)] for x=0.05 and x=0.15 ceramics.

The activation energy (E_a) is calculated by Arrhenius formation [23]:

$$\sigma = \sigma_0 \exp\left(\frac{E_a}{kT}\right) \#(11)$$

where σ_0 represents the pre-exponent constant, σ ($=1/\rho$ (ρ is resistivity)) indicates the bulk conductivity, k is the Boltzmann constant, and T is the Kelvin temperature. The E_a can be determined from the slope of ln(1/R)-1000/T. Compared with x=0.05 sample, the larger radius of the semicircle arc for impedance spectra can be observed in x=0.15 ceramic (Fig. S25(a), (b)), demonstrating good electrical insulation characteristics. As shown in Fig. S25(c), (d), a higher E_a value (~ 1.86 eV) for the ceramic with x=0.15 also confirms its strong electrical insulating properties arising from a lower oxygen vacancy concentration.
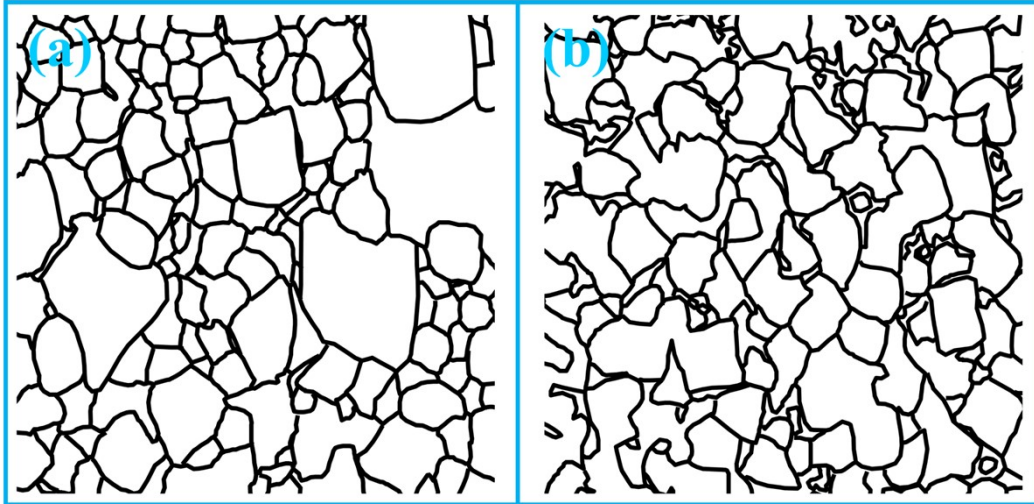
Fig. S26 Simulation models for (a) x=0.05 and (b) x=0.15 ceramics.

To ensure the most realistic simulated results, the intrinsic (dielectric constant) and external (grain and grain boundary distribution) factors of the ceramics are mainly considered for the two-dimensional model.
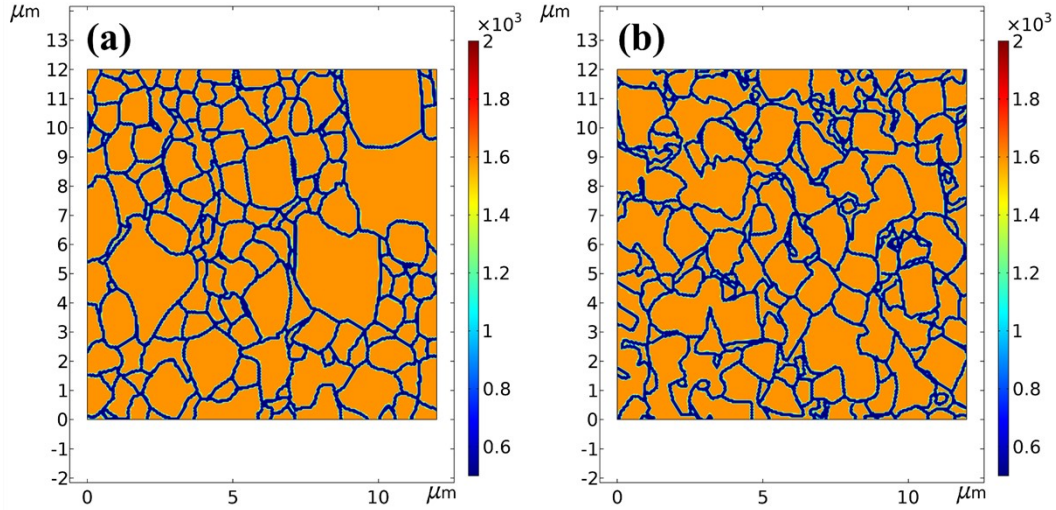
Fig. S27 Distribution of dielectric constant for (a) x=0.05 and (b) x=0.15 ceramics.

The dielectric constant of the grain and grain boundary can be determined by the structural model proposed by Randall et al. [3], which are expressed as follows:

$$\frac{1}{\varepsilon'} = \frac{1}{\varepsilon'_g} + \frac{1}{k\varepsilon'_{gb}} \#(12)$$

where ε', ε'_g and ε'_{gb} represent the dielectric constant of the ceramics, grain and grain boundary, respectively. In this study, the region of 12 μm × 12 μm was chosen to establish the corresponding simulation model based on the SEM micrographs of the sample. In detail, a thickness is 12 μm for samples, and a volage of 420 V (~ 350 kV/cm) was applied to conduct the simulation.
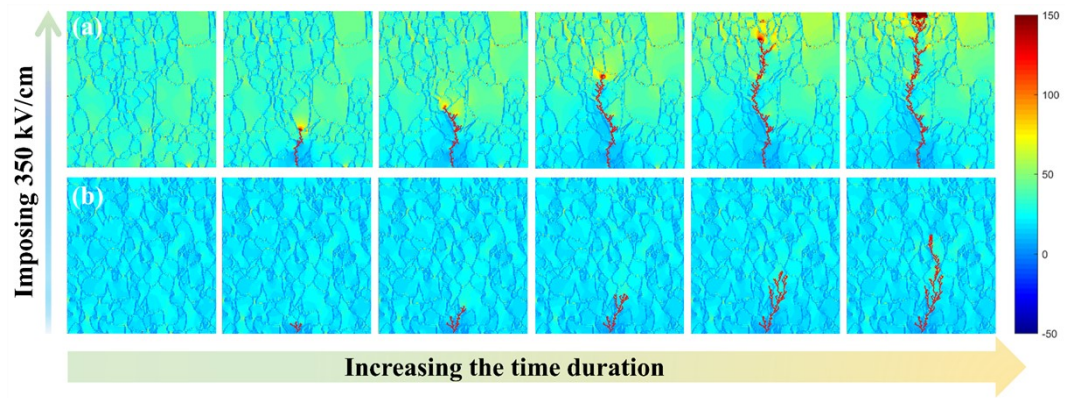
Fig. S28 The polarization distribution with electric tree evolution for (a) x=0.05 and (b) x=0.15 ceramics.

Table S1 A comparison of x=0.15 ceramic with recently reported lead-free ceramics on E_b, W_{rec}, η, W_{rec} /E_b.

Compositions	E_b (kV/cm)	W_{rec} (J/cm^3)	η (%)	W_{rec}/E_b (μC/cm^2)	Ref.
0.9(Sr$_{0.7}$Bi$_{0.2}$)TiO$_3$-0.1Bi(Mg$_{0.5}$Hf$_{0.5}$)O$_3$	360	3.1	93	0.00861	[24]
SrTi$_{0.985}$(Zn$_{1/3}$Nb$_{2/3}$)$_{0.015}$O$_3$-4.5 wt%ZnNb$_2$O$_6$	422	2.35	77	0.00557	[25]
Sr$_{0.92}$Dy$_{0.08}$TiO$_3$	510	4	89.5	0.00784	[26]
0.8ST-0.2(NBT-Ba$_{0.94}$La$_{0.04}$Zr$_{0.02}$Ti$_{0.98}$O$_3$)	320	2.83	85	0.00884	[27]
Sr$_{0.7}$Bi$_{0.2}$TiO$_3$	543	5.21	91.55	0.00959	[28]
0.88SBT-0.12BNN	580	5.98	98.6	0.01031	[13]
0.98(SBT-BNT)-0.02BMT	560	8	91	0.01429	[29]
0.2SNBCT	440	6	92	0.01364	[30]
0.43BiFeO$_3$-0.45SrTiO$_3$-0.12BaTiO$_3$	504	7.3	86.3	0.01448	[31]
0.6BT-0.4Bi(Mg$_{0.5}$Ti$_{0.5}$)O$_3$	340	4.49	93	0.01321	[32]
0.65(Ba$_{0.98}$Li$_{0.04}$)Ti$_{0.98}$O$_3$-0.35(Sr$_{0.7}$Bi$_{0.2}$)TiO$_3$	410	3.54	75.6	0.00863	[33]
0.87BaTiO$_3$-0.13Bi(Zn$_{2/3}$(Nb$_{0.85}$Ta$_{0.15}$)$_{1/3}$)O$_3$	790	5.04	68	0.00638	[34]
BT-BMZ@SiO$_2$	345	3.41	85.1	0.00988	[35]
BT-BZT-0.3BNT	230	4.18	84.01	0.01817	[36]
0.85KNN-0.15Bi(Zn$_{0.5}$Zr$_{0.5}$)O$_3$	326	3.5	86.8	0.01074	[37]
0.85K$_{0.5}$Na$_{0.5}$NbO$_3$-0.15Bi(Zn$_{2/3}$Ta$_{1/3}$)O$_3$	600	6.7	92	0.01117	[38]
0.80KNN-0.20ST	400	3.67	72.1	0.00917	[39]
0.90KNN-0.10BMN	300	4.08	62.7	0.0136	[40]

0.9KNN-0.1BMN-1.0 mol %CuO	400	4.02	57.3	0.01005	41
$Ag_{0.94}La_{0.02}NbO_3$	273	4.4	73	0.01612	42
$Ag_{0.88}Gd_{0.04}NbO_3$	290	4.5	64	0.01552	43
$Ag_{0.92}Ca_{0.04}NbO_3$	220	3.55	56.3	0.01614	44
$Ag_{0.91}Sm_{0.03}NbO_3$	290	5.2	68.5	0.01793	45
$Ag_{0.97}Nd_{0.01}Ta_{0.2}Nb_{0.8}O_3$	370	6.5	71	0.01757	46
$0.45AgNbO_3$-$0.55AgTaO_3$	470	6.3	90	0.0134	11
$AgNbO_3$	270	3.34	54.5	0.01237	47
$BiFeO_3$-$BaTiO_3$-$Na_{0.73}Bi_{0.09}NbO_3$	410	5.57	83.8	0.01359	48
0.61BF-0.33BST-$0.06La(Mg_{2/3}Nb_{1/3})O_3$	230	3.38	59	0.0147	49
0.7(0.67BF-0.34BT)-$0.3(Sr_{0.7}Bi_{0.2})TiO_3$	180	2.4	90.4	0.01333	50
0.57BF-0.30BT-0.13 $Bi(Li_{0.5}Nb_{0.5})O_3$	280	3.64	74	0.013	51
$0.67Bi_{0.9}Sm_{0.1}FeO_3$-0.33BT	200	2.8	55.8	0.014	52
$Na_{0.7}Bi_{0.1}Nb_{0.9}Ta_{0.1}O_3$	530	7.33	83.68	0.01383	53
$0.91NN$-$0.09Bi(Zn_{0.5}Ti_{0.5})O_3$	250	2.2	62.7	0.0088	54
$(Na_{0.84}Bi_{0.08})(Nb_{0.92}Zr_{0.08})O_3$+CuO	430	4.9	88	0.0114	55
0.92NN-$0.08Bi(Mg_{0.5}Ti_{0.5})O_3$+$MnO_2$	480	5.57	71	0.0116	56
$(Na_{0.91}La_{0.09})(Nb_{0.82}Ti_{0.18})O_3$	550	6.5	66	0.01182	57
$0.84NaNbO_3$-$0.06BiFeO_3$-$0.1SrTiO_3$	380	5.29	82.1	0.01392	58
$0.9NaNbO_3$-$0.1Bi(Zn_{0.5}Sn_{0.5})O_3$	350	3.14	83.3	0.00897	59
$0.6(0.8Bi_{0.5}Na_{0.4}K_{0.1}TiO_3$-	260	4.44	81.8	0.01708	60

0.2SrTiO$_3$)-0.4NaNbO$_3$					
0.75Bi$_{0.58}$Na$_{0.42}$TiO$_3$-0.25ST	535	5.63	94	0.01052	[61]
0.62NBT-0.30SBT-0.08BMN	470	7.5	92	0.01596	[62]
0.9(0.75BNT-0.25ST)-0.1Ag(Nb$_{0.85}$Ta$_{0.15}$)O$_3$	290	3.6	80	0.01241	[63]
0.78BNT-0.22NN	390	7.02	85	0.018	[64]
0.8BNT-0.2NaTaO$_3$	380	4.21	77.8	0.01108	[65]
0.80Bi$_{0.5}$Na$_{0.5}$TiO$_3$-0.20SrNb$_{0.5}$Al$_{0.5}$O$_3$	565	7	95	0.01239	[66]
0.85Bi$_{0.5}$Na$_{0.5}$TiO$_3$-0.15AgNb$_{0.5}$Ta$_{0.5}$O$_3$	518	6.6	72	0.01274	[15]
0.88(0.65Bi$_{0.5}$Na$_{0.5}$TiO$_3$-0.35SrTiO$_3$)-0.12Bi(Mg$_{0.5}$Hf$_{0.5}$)O$_3$	390	5.59	85.3	0.01433	[16]
BNT-BT-0.12La	440	6.69	87	0.0152	[67]
0.9BNT-0.1LiTaO$_3$	200	3.1	74.2	0.0155	[68]
BNT-BAT-0.15BMN	420	6.3	79.6	0.015	[69]
BNT-BAT-0.7SBNLT	200	2.03	72	0.01015	[70]
(Ca$_{0.5}$Sr$_{0.5}$)$_{0.8875}$La$_{0.075}$TiO$_3$	370	2.07	93	0.00559	[71]
Ca$_{0.5}$Sr$_{0.5}$Ti$_{0.85}$Zr$_{0.15}$O$_3$	440	3.37	96	0.00766	[72]
0.6BKT-0.3BT-0.1NN	460	7.57	81.4	0.01646	[8]
0.76BKT-0.24BF	150	2.88	76.9	0.0192	[73]
BKTBFO-0.16NSN	425	6.52	70	0.01534	[74]
BKT-0.15BMN	230	3.14	83.7	0.01365	[75]
BNT-BAT-0.15NT	**420**	**6.82**	**90**	**0.01624**	**This work**

Table S2 A comparison of temperature stability between this work and other recently reported lead-free ceramics.

Num.	Compositions	Temperature (°C)	W_{rec} (J/cm^3)	Ref.
1	$Ba_{0.82}Bi_{0.12}TiO_3$	30-120	3.21-3.35	[76]
2	KNN-H	25-140	3.18-3.58	[9]
3	CT-0.2(BNT-BAT)	20-160	3.9-4.3	[77]
4	BNT-BT-0.12La	25-180	1.49-1.73	[67]
5	BT-BMZ@SiO$_2$	30-150	2.68-2.74	[35]
6	0.78NN-0.22BMT	20-200	2.11-2.29	[78]
7	0.76KBT-0.24BF	20-160	1.222-1.357	[73]
8	NKSN-SZ-0.14BNZ	0-200	3.3-3.46	[79]
9	BF-BT-0.3SST	25-110	0.62-0.652	[80]
10	0.6BKT-0.3BT-0.1NN	20-200	4.06-4.58	[8]
11	**BNT-BAT-0.15NT**	**20-160**	**3.35-3.73**	**This work**

Table S3 A comparison of W_D, P_D, and $t_{0.9}$ among this work and other recently reported lead-free ceramics.

Compositions	W_D (J/cm³)	P_D (MW/cm³)	$t_{0.9}$ (ns)	Ref.
NN-BMT	1.17	63.7	85	[56]
BNT-BAT-CT	0.72	96.2	37.6	[21]
BNT-SLT	2.31	182	123	[81]
NN-BMN	0.47	47.6	45	[82]
SBKT+Er$_2$O$_3$	1.51	39.6	325	[83]
NN-CT	0.88	114.8	45	[84]
BNT-LT	0.51	22	100	[68]
SBT-KBT	1.81	49.5	360	[85]
BNST-STZ	1.17	41.2	125.6	[86]
BNT-BAT-0.15NT	**1.69**	**122**	**97**	**This Work**

Table S4 Multidimensional comparisons of comprehensive properties including W_{rec}, η, W_{rec}/E_b, thermal, and frequency stability between this work and representative lead-free energy storage ceramics with superior comprehensive performance.

Compositions	W_{rec} (J/cm³)	η (%)	W_{rec}/E_b (μC/cm²)	Temperature (°C)	Frequency (Hz)	Ref.
KNN-BZT	6.7	92	0.01117	25-150	1-100	[38]
BKT-BT-NN	7.57	81.4	0.01646	20-200	5-100	[8]
AN-AT	6.3	90	0.0134	20-150		[11]
NN-BF-ST	5.29	82.1	0.01392	20-120	1-200	[58]
BF-BST-BZN	7.4	81	0.01088	30-130	1-200	[87]
BNT-BAT-0.15NT	**6.82**	**90**	**0.01624**	**20-160**	**1-500**	**This work**

References

1. H. Pan, J. Ma, J. Ma, Q. Zhang, X. Liu, B. Guan, L. Gu, X. Zhang, Y.-J. Zhang, L. Li, Y. Shen, Y.-H. Lin and C.-W. Nan, *Nat. Commun.*, 2018, **9**, 1813.

2. H. Bai, K. Zhu, Z. Wang, B. Shen and J. Zhai, *Adv. Funct. Mater.*, 2021, **31**, 2102646.

3. F. Yan, H. Bai, G. Ge, J. Lin, C. Shi, K. Zhu, B. Shen, J. Zhai and S. Zhang, *Small*, 2022, **18**, 2106515.

4. Y. Gao, X. Zhu, B. Yang, P. Shi, R. Kang, Y. Yuan, Q. Liu, M. Wu, J. Gao and X. Lou, *Chem. Eng. J.*, 2022, **433**, 133584.

5. X. Zhu, Y. Gao, P. Shi, R. Kang, F. Kang, W. Qiao, J. Zhao, Z. Wang, Y. Yuan and X. Lou, *Nano Energy*, 2022, **98**, 107276.

6. H. Pan, S. Lan, S. Xu, Q. Zhang, H. Yao, Y. Liu, F. Meng, E.-J. Guo, L. Gu, D. Yi, X. Renshaw Wang, H. Huang, J. L. MacManus-Driscoll, L.-Q. Chen, K.-J. Jin, C.-W. Nan and Y.-H. Lin, *Science*, 2021, **374**, 100-104.

7. L. Yang, X. Kong, F. Li, H. Hao, Z. Cheng, H. Liu, J.-F. Li and S. Zhang, *Prog. Mater. Sci.*, 2019, **102**, 72-108.

8. L. Chen, F. Long, H. Qi, H. Liu, S. Deng and J. Chen, *Adv. Funct. Mater.*, 2022, **32**, 2110478.

9. L. Chen, S. Deng, H. Liu, J. Wu, H. Qi and J. Chen, *Nat. Commun.*, 2022, **13**, 3089.

10. J. Li, Z. Shen, X. Chen, S. Yang, W. Zhou, M. Wang, L. Wang, Q. Kou, Y. Liu, Q. Li, Z. Xu, Y. Chang, S. Zhang and F. Li, *Nat. Mater.*, 2020, **19**, 999-1005.

11. N. Luo, K. Han, M. J. Cabral, X. Liao, S. Zhang, C. Liao, G. Zhang, X. Chen, Q. Feng, J.-F. Li and Y. Wei, *Nat. Commun.*, 2020, **11**, 4824.

12. A. Xie, R. Zuo, Z. Qiao, Z. Fu, T. Hu and L. Fei, *Adv. Energy Mater.*, 2021, **11**, 2101378.

13. J. Liu, Y. Ding, C. Li, W. Bai, P. Zheng, S. Wu, J. Zhang, Z. Pan and J. Zhai, *J. Mater. Chem. A*, 2023, **11**, 609-620.

14. Z.-N. Guan, Y. Yan, J. Ma, T. Pan, X. Li, S. Guo, J. Zhang, J. Wang and Y. Wang, *ACS Appl. Mater. Interfaces*, 2022, **14**, 44539-44549.

15. Z. Che, L. Ma, G. Luo, C. Xu, Z. Cen, Q. Feng, X. Chen, K. Ren and N. Luo,

Nano Energy, 2022, **100**, 107484.

16. X. Zhu, P. Shi, Y. Gao, R. Kang, J. Zhao, A. Xiao, W. Qiao, J. Zhao, Z. Wang and X. Lou, *Chem. Eng. J.*, 2022, **437**, 135462.

17. T. Tunkasiri and G. Rujijanagul, *J Mater Sci Lett*, 1996, **15**, 1767-1769.

18. C. Pascual-Gonzalez, G. Schileo, S. Murakami, A. Khesro, D. Wang, I. M. Reaney and A. Feteira, *Appl. Phys. Lett.*, 2017, **110**, 172902.

19. H. Pan, F. Li, Y. Liu, Q. Zhang, M. Wang, S. Lan, Y. Zheng, J. Ma, L. Gu, Y. Shen, P. Yu, S. Zhang, L.-Q. Chen, Y.-H. Lin and C.-W. Nan, *Science*, 2019, **365**, 578-582.

20. B. Yang, Y. Zhang, H. Pan, W. Si, Q. Zhang, Z. Shen, Y. Yu, S. Lan, F. Meng, Y. Liu, H. Huang, J. He, L. Gu, S. Zhang, L.-Q. Chen, J. Zhu, C.-W. Nan and Y.-H. Lin, *Nat. Mater.*, 2022, **21**, 1074-1080.

21. C. Li, J. Liu, W. Bai, S. Wu, P. Zheng, J. Zhang, Z. Pan and J. Zhai, *J. Mater. Chem. A*, 2022, **10**, 9535-9546.

22. C. Kim, G. Pilania and R. Ramprasad, *Journal of Physical Chemistry C*, 2016, **120**, 14575-14580.

23. K. J. Laidler, *J Chem Educ*, 1984, **61**, 494.

24. X. Kong, L. Yang, Z. Cheng and S. Zhang, *J. Am. Ceram. Soc.*, 2020, **103**, 1722-1731.

25. W. Pan, M. Cao, A. Jan, H. Hao, Z. Yao and H. Liu, *J. Mater. Chem. C*, 2020, **8**, 2019-2027.

26. X. Guo, Y. Pu, W. Wang, J. Ji, J. Li, R. Shi and M. Yang, *Ceram. Int.*, 2020, **46**, 21719-21727.

27. H. Yang, F. Yan, Y. Lin and T. Wang, *ACS Sustain. Chem. Eng.*, 2017, **5**, 10215-10222.

28. C. Zuo, S. Yang, Z. Cao, H. Yu and X. Wei, *Chem. Eng. J.*, 2022, **442**, 136330.

29. Z. Wang, R. Kang, Z. Hong, X. Ke, X. Lou, L. Zhang, L. Zhang and J. Wang, *ACS Appl. Mater. Interfaces*, 2022, **14**, 44389-44397.

30. L. Liu, Y. Liu, J. Hao, J. Chen, P. Li, S. Chen, P. Fu, W. Li and J. Zhai, *Nano Energy*, 2023, **109**, 108275.

31. T. Cui, A. Yu, Y. Zhang, J. Guo, X. Li, S. Guo, J. Zhang, J. Wang and S.-T. Zhang, *J. Am. Ceram. Soc.*, 2022, **105**, 6252-6261.

32. Q. Hu, Y. Tian, Q. Zhu, J. Bian, L. Jin, H. Du, D. O. Alikin, V. Y. Shur, Y. Feng, Z. Xu and X. Wei, *Nano Energy*, 2020, **67**, 104264.

33. G. Liu, Y. Li, B. Guo, M. Tang, Q. Li, J. Dong, L. Yu, K. Yu, Y. Yan, D. Wang, L. Zhang, H. Zhang, Z. He and L. Jin, *Chem. Eng. J.*, 2020, **398**, 125625.

34. Z. Cai, C. Zhu, H. Wang, P. Zhao, Y. Yu, L. Li and X. Wang, *J. Mater. Chem. A*, 2019, **7**, 17283-17291.

35. Q. Yuan, F.-Z. Yao, S.-D. Cheng, L. Wang, Y. Wang, S.-B. Mi, Q. Wang, X. Wang and H. Wang, *Adv. Funct. Mater.*, 2020, **30**, 2000191.

36. W. Qin, M. Zhao, Z. Li, D. Zhang, M. Zhang, Y. Xu, L. Jin and Y. Yan, *Chem. Eng. J.*, 2022, **443**, 136505.

37. M. Zhang, H. Yang, D. Li, L. Ma and Y. Lin, *J. Mater. Chem. C*, 2020, **8**, 8777-8785.

38. D. Li, D. Zhou, D. Wang, W. Zhao, Y. Guo and Z. Shi, *Adv. Funct. Mater.*, 2022, **32**, 2111776.

39. Z. Yang, H. Du, S. Qu, Y. Hou, H. Ma, J. Wang, J. Wang, X. Wei and Z. Xu, *J. Mater. Chem. A*, 2016, **4**, 13778-13785.

40. T. Shao, H. Du, H. Ma, S. Qu, J. Wang, J. Wang, X. Wei and Z. Xu, *J. Mater. Chem. A*, 2017, **5**, 554-563.

41. X. Lu, L. Zhang, H. Talebinezhad, Y. Tong and Z. Y. Cheng, *Ceram. Int.*, 2018, **44**, 16977-16983.

42. J. Gao, Y. Zhang, L. Zhao, K.-Y. Lee, Q. Liu, A. Studer, M. Hinterstein, S. Zhang and J.-F. Li, *J. Mater. Chem. A*, 2019, **7**, 2225-2232.

43. S. Li, H. Nie, G. Wang, C. Xu, N. Liu, M. Zhou, F. Cao and X. Dong, *J. Mater. Chem. C*, 2019, **7**, 1551-1560.

44. N. Luo, K. Han, F. Zhuo, L. Liu, X. Chen, B. Peng, X. Wang, Q. Feng and Y. Wei, *J. Mater. Chem. C*, 2019, **7**, 4999-5008.

45. N. Luo, K. Han, F. Zhuo, C. Xu, G. Zhang, L. Liu, X. Chen, C. Hu, H. Zhou and Y. Wei, *J. Mater. Chem. A*, 2019, **7**, 14118-14128.

46. Z. Lu, W. Bao, G. Wang, S.-K. Sun, L. Li, J. Li, H. Yang, H. Ji, A. Feteira, D. Li, F. Xu, A. K. Kleppe, D. Wang, S.-Y. Liu and I. M. Reaney, *Nano Energy*, 2021, **79**, 105423.

47. J. Huang, X. Hou, S. Gao, Y. Zhou, H. Huang, Y. He and Q. Zhang, *J. Mater. Chem. A*, 2022, **10**, 16337-16350.

48. F. Yan, Y. Shi, X. Zhou, K. Zhu, B. Shen and J. Zhai, *Chem. Eng. J.*, 2021, **417**, 127945.

49. H. Yang, H. Qi and R. Zuo, *J. Eur. Ceram. Soc.*, 2019, **39**, 2673-2679.

50. Z. Chen, X. Bu, B. Ruan, J. Du, P. Zheng, L. Li, F. Wen, W. Bai, W. Wu, L. Zheng and Y. Zhang, *J. Eur. Ceram. Soc.*, 2020, **40**, 5450-5457.

51. G. Wang, Z. Lu, H. Yang, H. Ji, A. Mostaed, L. Li, Y. Wei, A. Feteira, S. Sun, D. C. Sinclair, D. Wang and I. M. Reaney, *J. Mater. Chem. A*, 2020, **8**, 11414-11423.

52. Z. Chen, X. Bai, H. Wang, J. Du, W. Bai, L. Li, F. Wen, P. Zheng, W. Wu, L. Zheng and Y. Zhang, *Ceram. Int.*, 2020, **46**, 11549-11555.

53. W. Yang, H. Zeng, F. Yan, J. Lin, G. Ge, Y. Cao, W. Du, K. Zhao, G. Li, H. Xie and J. Zhai, *J. Mater. Chem. A*, 2022, **10**, 11613-11624.

54. Y. Fan, Z. Zhou, R. Liang and X. Dong, *J. Eur. Ceram. Soc.*, 2019, **39**, 4770-4777.

55. L. Yang, X. Kong, Z. Cheng and S. Zhang, *ACS Appl. Mater. Interfaces*, 2020, **12**, 32834-32841.

56. A. Tian, R. Zuo, H. Qi and M. Shi, *J. Mater. Chem. A*, 2020, **8**, 8352-8359.

57. J. Chen, H. Qi and R. Zuo, *ACS Appl. Mater. Interfaces*, 2020, **12**, 32871-32879.

58. X. Wang, X. Wang, Y. Huan, C. Li, J. Ouyang and T. Wei, *ACS Appl. Mater. Interfaces*, 2022, **14**, 9330-9339.

59. X. Dong, X. Li, H. Chen, Q. Dong, J. Wang, X. Wang, Y. Pan, X. Chen and H. Zhou, *J. Adv. Ceram.*, 2022, **11**, 729-741.

60. W. Shi, Y. Yang, L. Zhang, R. Jing, Q. Hu, D. O. Alikin, V. Y. Shur, J. Gao, X. Wei and L. Jin, *Ceram. Int.*, 2022, **48**, 6512-6519.

61. F. Yan, K. Huang, T. Jiang, X. Zhou, Y. Shi, G. Ge, B. Shen and J. Zhai, *Energy Stor. Mater.*, 2020, **30**, 392-400.

62. H. Ji, D. Wang, W. Bao, Z. Lu, G. Wang, H. Yang, A. Mostaed, L. Li, A. Feteira,

S. Sun, F. Xu, D. Li, C.-J. Ma, S.-Y. Liu and I. M. Reaney, *Energy Stor. Mater.*, 2021, **38**, 113-120.

63. T. Li, P. Chen, F. Li and C. Wang, *Chem. Eng. J.*, 2021, **406**, 127151.

64. H. Qi and R. Zuo, *J. Mater. Chem. A*, 2019, **7**, 3971-3978.

65. X. Zhou, H. Qi, Z. Yan, G. Xue, H. Luo and D. Zhang, *ACS Appl. Mater. Interfaces*, 2019, **11**, 43107-43115.

66. F. Yan, H. Bai, G. Ge, J. Lin, K. Zhu, G. Li, J. Qian, B. Shen, J. Zhai and Z. Liu, *Small*, 2022, **18**, 2202575.

67. B. Chu, J. Hao, P. Li, Y. Li, W. Li, L. Zheng and H. Zeng, *ACS Appl. Mater. Interfaces*, 2022, **14**, 19683-19696.

68. L. Zhang, Y. Pu, M. Chen, T. Wei and X. Peng, *Chem. Eng. J.*, 2020, **383**, 123154.

69. B. Guo, Y. Yan, M. Tang, Z. Wang, Y. Li, L. Zhang, H. Zhang, L. Jin and G. Liu, *Chem. Eng. J.*, 2021, **420**, 130475.

70. J. Liu, Y. Ding, C. Li, W. Bai, P. Zheng, J. Zhang and J. Zhai, *J. Mater. Sci. Mater. Electron.*, 2021, **32**, 21164-21177.

71. W. Wang, Y. Pu, X. Guo, T. Ouyang, Y. Shi, M. Yang, J. Li, R. Shi and G. Liu, *Ceram. Int.*, 2019, **45**, 14684-14690.

72. Y. Pu, W. Wang, X. Guo, R. Shi, M. Yang and J. Li, *J. Mater. Chem. C*, 2019, **7**, 14384-14393.

73. Q. Yang, M. Zhu, Q. Wei, M. Zhang, M. Zheng and Y. Hou, *Chem. Eng. J.*, 2021, **414**, 128769.

74. H. Wang, E. Li, K. Wei, H. Li, M. Xing and C. Zhong, *ACS Appl. Mater. Interfaces*, 2022, **14**, 54021-54033.

75. F. Li, X. Hou, T. Li, R. Si, C. Wang and J. Zhai, *J. Mater. Chem. C*, 2019, **7**, 12127-12138.

76. Z. Sun, J. Zhang, H. Luo, Y. Yao, N. Wang, L. Chen, T. Li, C. Hu, H. Qi, S. Deng, L. C. Gallington, Y. Zhang, J. C. Neuefeind, H. Liu and J. Chen, *J. Am. Chem. Soc.*, 2023, **145**, 6194-6202.

77. C. Li, J. Liu, L. Lin, W. Bai, S. Wu, P. Zheng, J. Zhang and J. Zhai, *Small*, 2023, **19**, 2206662.

78. J. Shi, X. Chen, X. Li, J. Sun, C. Sun, F. Pang and H. Zhou, *J. Mater. Chem. C*, 2020, **8**, 3784-3794.

79. A. Xie, J. Fu, R. Zuo, X. Jiang, T. Li, Z. Fu, Y. Yin, X. Li and S. Zhang, *Adv. Mater.*, 2022, **34**, 2204356.

80. S. Liu, W. Feng, J. Li, B. He, M. Liu, Z. Bao, D. Luo and C. Zhao, *J. Eur. Ceram. Soc.*, 2022, **42**, 7430-7440.

81. X. Qiao, F. Zhang, D. Wu, B. Chen, X. Zhao, Z. Peng, X. Ren, P. Liang, X. Chao and Z. Yang, *Chem. Eng. J.*, 2020, **388**, 124158.

82. C. Sun, X. Chen, J. Shi, F. Pang, X. Dong, H. y. Chen, K. Wang, X. Zhou and H. Zhou, *J. Eur. Ceram. Soc.*, 2021, **41**, 1891-1903.

83. P. Zhao, B. Tang, Z. Fang, F. Si, C. Yang and S. Zhang, *Chem. Eng. J.*, 2021, **403**, 126290.

84. J. Liu, P. Li, C. Li, W. Bai, S. Wu, P. Zheng, J. Zhang and J. Zhai, *ACS Appl. Mater. Interfaces*, 2022, **14**, 17662-17673.

85. P. Zhao, B. Tang, Z. Fang, F. Si, C. Yang, G. Liu and S. Zhang, *J. Materiomics*, 2021, **7**, 195-207.

86. D. Li, Y. Lin, M. Zhang and H. Yang, *Chem. Eng. J.*, 2020, **392**, 123729.

87. J. Zhao, T. Hu, Z. Fu, Z. Pan, L. Tang, X. Chen, H. Li, J. Hu, L. Lv, Z. Zhou, J. Liu, P. Li and J. Zhai, *Small*, 2023, **19**, 2206840.